Available online at www.sciencedirect.com

ScienceDirect

Publishing Services by Elsevier

International Journal of Naval Architecture and Ocean Engineering 10 (2018) 329–347
http://www.journals.elsevier.com/international-journal-of-naval-architecture-and-ocean-engineering/

An improved solid boundary treatment for wave–float interactions using ISPH method

Xing Zheng [a,*], Xipeng Lv [a], Qingwei Ma [b], Wenyang Duan [a], Abbas Khayyer [c], Songdong Shao [d,e]

[a] College of Shipbuilding Engineering, Harbin Engineering University, Harbin 150001, China
[b] School of Mathematics, Computer Science and Engineering, City, University of London, London EC1V 0HB, UK
[c] Department of Civil and Earth Resources Engineering, Kyoto University, Kyoto 615-8540, Japan
[d] Department of Civil and Structural Engineering, University of Sheffield, Sheffield S1 3JD, UK
[e] State Key Laboratory of Hydro-Science and Engineering, Tsinghua University, Beijing 100084, China

Received 17 March 2017; revised 1 July 2017; accepted 1 August 2017
Available online 12 September 2017

Abstract

The Smoothed Particle Hydrodynamics (SPH) method has proved to have great potentials in dealing with the wave-structure interactions. Compared with the Weakly Compressible SPH (WCSPH) method, the ISPH approach solves the pressure by using the pressure Poisson equation rather than the equation of state. This could provide a more stable and accurate pressure field that is important in the study of wave-structure interactions. This paper improves the solid boundary treatment of ISPH by using a high accuracy Simplified Finite Difference Interpolation (SFDI) scheme for the 2D wave-structure coupling problems, especially for free-moving structure. The proposed method is referred as the ISPH_BS. The model improvement is demonstrated by the documented benchmark tests and laboratory experiment covering various wave-structure interaction applications.
Copyright © 2017 Society of Naval Architects of Korea. Production and hosting by Elsevier B.V. This is an open access article under the CC BY-NC-ND license (http://creativecommons.org/licenses/by-nc-nd/4.0/).

Keywords: ISPH; Moving boundary; SFDI; Wave–float interactions; ISPH_BS

1. Introduction

The research of wave action on structure has drawn wide attentions, especially in the coastal and ocean engineering. People have made numerous efforts in the study of moving object in the waves, and proposed a variety of approaches to investigate the interaction between the wave and the object. From the simple Morrison formula to the advanced 3D Reynolds-Averaged Navier–Stokes equations (RANS) model (Lin and Liu, 1998), the researchers have developed different theoretical and numerical modelling approaches. The early Boundary Element Method (BEM) based on the frequency domain theorem could solve the motion of floating body in a linear wave with sufficient accuracy. However, they could not perform satisfactorily in the more complex and common nonlinear wave field. To partially solve the problem, Faltinsen (1977) proposed a mixed Eulerian–Lagrangian Boundary Element method to investigate the interaction between the wave and a rigid body, but could not capture the large deformation of free surface under the wave breaking. Afterwards the mesh-based Navier–Stokes (N–S) numerical models have been used to overcome the deficiency of previous approaches, but they need additional tracking algorithm to describe the free surface. Since these methods are based on a fixed Eulerian grid, the treatment of free surface is complex in the violent breaking waves and during the wave-structure interactions.

In the past two decades, the Smoothed Particle Hydrodynamics (SPH) method has emerged as a promising mesh-free Lagrangian modelling technique in many areas of solid and fluid dynamics. Monaghan et al. (2003) used the WCSPH to

* Corresponding author.
E-mail address: zhengxing@hrbeu.edu.cn (X. Zheng).
Peer review under responsibility of Society of Naval Architects of Korea.

http://dx.doi.org/10.1016/j.ijnaoe.2017.08.001
2092-6782/Copyright © 2017 Society of Naval Architects of Korea. Production and hosting by Elsevier B.V. This is an open access article under the CC BY-NC-ND license (http://creativecommons.org/licenses/by-nc-nd/4.0/).

investigate the water entry of a box travelling down the slope. Najafi-Jilani and Rezaie-Mazyak (2011) used the SPH to study the movement of a floating breakwater. Bouscasse et al. (2013) modelled the interactions between a 2D box and a wave packet by using the ghost-fluid technique on the solid surface. Canelas et al. (2015) used the noise-free δ-SPH on the unsteady motion of bodies through a free surface. Jun et al. (2015) carried out a comprehensive dynamic analysis of floating body in the fluids combining the SPH with physical experiment. Ren et al. (2015) used the WCSPH to analyse the wave-induced motion of a freely floating body. In the latest practical SPH applications, Rudman and Cleary (2016) studied the impact of a rogue wave on the moored floating offshore structure with a focus on the effect that different mooring systems have on the platform. Besides, Gomez-Gesteira et al. (2012) published the open source code SPHysics with case examples on the wave–float interaction. To improve the pressure prediction, the Incompressible SPH (ISPH) method has also been used in the wave-structure interactions with a promising performance in the computational accuracy and stability. For example, Asai et al. (2012) developed a stabilized ISPH pressure solution with the eddy viscosity and relaxation coefficient to calculate the free water entry of a falling object. Liu et al. (2014) used the ISPH to simulate the coupled structure interactions with a free surface flow based on an improved mirror particle boundary. Gotoh et al. (2014) developed an enhanced ISPH scheme to study the violent sloshing flow based on a higher-order Laplacian and error compensating source term. Aly et al. (2015) proposed a stabilized ISPH pressure solution method with a density-invariant relaxation condition to simulate the highly nonlinear liquid sloshings. In addition, Ikari et al. (2011) used a Moving Particle Semi-implicit (MPS) method to predict the mooring forces on a floating body. Further improvement on MPS has been done by Lee et al. (2013) for the simulation of nonlinear floating-body motions. The state-of-the-art review on the projection-based particle methods and wave-structure interactions has been provided by Gotoh and Khayyer (2016). It should be mentioned that the pioneering work on wave–float interaction using the mesh-free particle modelling approach should be attributed to Koshizuka et al. (1998).

Although the ISPH approach could predict better pressure field than the WCSPH does, the numerical accuracy and efficiency could be compromised when the solid boundary is complex for the wave-structure interaction especially with the moving boundary. This is due to that the accurate implementation of boundary condition for the pressure Poisson equation becomes more challenging. In order to improve the kernel approximation near the solid boundary, many researchers have made efforts. Liu et al. (1995) proposed the reproducing kernel particle method to improve the accuracy of particle approximations. Bonet and Lok (1999) introduced a renormalized kernel function approach by use of a variational framework. Dilts (1999) resorted to the moving-least-square particle hydrodynamics. Quinlan et al. (2006) investigated the effect of kernel functions and support domains with corrected kernel approximations. Liu and Liu (2006) introduced a consistent kernel approximation to improve the accuracy of first-order derivative calculation. Oger et al. (2007) introduced a Taylor SPH scheme towards higher-order convergence. Ma (2008) introduced a Simplified Finite Difference Interpolation (SFDI) scheme to improve the particle approximation accuracy. Macia et al. (2011) carried out quite a few benchmark studies on the truncation error near the solid boundary.

The present paper proposes an improved solid boundary treatment for the wave–float interactions in the ISPH framework. The numerical treatment is based on the SFDI scheme originally developed by Sriram and Ma (2012) to increase the stability of pressure gradient calculation in MLPG_R, which was coupled with the ISPH solver for wave impact simulations (Zheng et al., 2014, 2017). However, the potentials of SFDI scheme have not been fully demonstrated in the wave-structure and wave–float interactions with the solid boundary effect. In the present study, we will use both the benchmark tests and self-designed laboratory experiment to show the promising performance of this technique in the SPH application field.

2. Review of ISPH methodology

2.1. SPH equations and solution algorithms

The Navier–Stokes equations are used to describe the fluid motion. In the incompressible SPH method, the fluid density is considered as a constant, and the mass and momentum conservation equations are written in the Lagrangian form as

$$\nabla \cdot \mathbf{u} = 0 \tag{1}$$

$$\frac{D\mathbf{u}}{Dt} = -\frac{1}{\rho}\nabla P + \mathbf{g} + \nu_0 \nabla^2 \mathbf{u} \tag{2}$$

where ρ is the fluid density; $\mathbf{u}$ is the particle velocity; t is the time; P is the particle pressure; $\mathbf{g}$ is the gravitational acceleration; and ν_0 is the kinematic viscosity. A two-step projection method is used to solve the velocity and pressure field from Eqs. (1) and (2). The first step is the prediction of velocity in the time domain without considering the pressure term. The intermediate particle velocity $\mathbf{u}_*$ and position $\mathbf{r}_*$ are obtained as

$$\mathbf{u}_* = \mathbf{u}_t + \Delta\mathbf{u}_* \tag{3}$$

$$\Delta\mathbf{u}_* = \left(\mathbf{g} + \nu_0 \nabla^2 \mathbf{u}\right)\Delta t \tag{4}$$

$$\mathbf{r}_* = \mathbf{r}_t + \mathbf{u}_* \Delta t \tag{5}$$

where $\mathbf{u}_t$ and $\mathbf{r}_t$ are the velocity and position at time t; Δt is the time step; $\Delta\mathbf{u}_*$ is the velocity increment; and $\mathbf{u}_*$ and $\mathbf{r}_*$ are the intermediate velocity and position.

The second step is the correction step, in which the pressure term is added, and $\Delta\mathbf{u}_{**}$ is the correction of particle velocity as

$$\Delta\mathbf{u}_{**} = -\frac{1}{\rho}\nabla P_{t+\Delta t}\Delta t \tag{6}$$

The following $\mathbf{u}_{t+\Delta t}$ and $\mathbf{r}_{t+\Delta t}$ represent the velocity and position of particle at the new time step, respectively.

$$\mathbf{u}_{t+\Delta t} = \mathbf{u}_* + \Delta \mathbf{u}_{**} \tag{7}$$

$$\mathbf{r}_{t+\Delta t} = \mathbf{r}_t + \frac{\mathbf{u}_t + \mathbf{u}_{t+\Delta t}}{2}\Delta t \tag{8}$$

Combining Eqs. (1) and (6), the following Poisson Equation of Pressure (PPE) is obtained

$$\nabla^2 P_{t+\Delta t} = \frac{\rho \nabla \cdot \mathbf{u}_*}{\Delta t} \tag{9}$$

Similarly, Shao and Lo (2003) proposed a projection-based incompressible approach by imposing the density invariance on each particle, leading to

$$\nabla \cdot \left(\frac{1}{\rho^*}\nabla P_{t+\Delta t}\right) = \frac{\rho_0 - \rho^*}{\rho_0 \Delta t^2} \tag{10}$$

where ρ^* is the density at the intermediate time step. Due to ρ^*/ρ_0 being very close to the unity, we can reasonably neglect their differences on the left and right-hand side of the denominator in Eq. (10), and obtain the combined PPE with both the divergence-free and density-invariance terms as

$$\nabla^2 P_{t+\Delta t} = \alpha \frac{\rho - \rho^*}{\Delta t^2} + (\alpha - 1)\frac{\rho \nabla \cdot \mathbf{u}_*}{\Delta t} \tag{11}$$

where α is a blending coefficient and a value of 0.01 is adopted in this paper based on the previous computational experiences. More in-depth study on the mixed PPE source term could be found in Zhang et al. (2006), Asai et al. (2012), Zheng et al. (2014) and Gui et al. (2015).

2.2. Calculation of spatial derivatives

The standard practice to calculate the gradient of pressure and the divergence of velocity is through the following Eqs. (12) and (13)

$$\nabla P_i = \rho_i \sum_{j=1}^{N} m_j \left(\frac{P_j}{\rho_j^2} + \frac{P_i}{\rho_i^2}\right) \nabla_i W\left(\left|\mathbf{r}_i - \mathbf{r}_j\right|, h\right) \tag{12}$$

$$\nabla \cdot \mathbf{u}_i = -\frac{1}{\rho_i} \sum_{j=1}^{N} m_j \mathbf{u}_{ij} \cdot \nabla_i W\left(\left|\mathbf{r}_i - \mathbf{r}_j\right|, h\right) \tag{13}$$

where $\mathbf{u}_{ij} = \mathbf{u}_i - \mathbf{u}_j$ is defined as the velocity difference; m is the particle mass; h is the kernel smoothing length; and i and j indicate the reference and neighbouring particles, respectively. $\nabla_i W$ is the gradient of SPH kernel function and a 2D cubic spline kernel is used in this paper. Here it should be noted that the mirror particle strategy, which will be discussed later, should be affected to some extent by the chosen kernel function.

The viscosity term in Eq. (2) adopts the following form

$$\nabla \cdot (\nu_i \nabla \mathbf{u}_i) = \sum_{j=1}^{N} 4 m_j \left(\frac{\nu_i + \nu_j}{\rho_i + \rho_j} \frac{\mathbf{u}_{ij} \cdot \mathbf{r}_{ij}}{\mathbf{r}_{ij}^2 + \eta^2}\right) \cdot \nabla_i W\left(\left|\mathbf{r}_i - \mathbf{r}_j\right|, h\right) \tag{14}$$

where $\eta^2 = 0.01h^2$ is a small parameter to avoid the singularity; and $\mathbf{r}_{ij} = \mathbf{r}_i - \mathbf{r}_j$ is defined as the position difference. The Laplacian term in Eqs. (10) or (11) can be discretisized by combining the SPH gradient and divergence rules as

$$\nabla \cdot \left(\frac{1}{\rho^*}\nabla P_{t+1}\right) = \sum_{j=1}^{N} m_j \frac{8}{\left(\rho_i + \rho_j\right)^2} \frac{P_{ij} \cdot \mathbf{r}_{ij}}{\mathbf{r}_{ij}^2 + \eta^2} \cdot \nabla_i W\left(\mathbf{r}_i - \mathbf{r}_j, h\right) \tag{15}$$

where $P_{ij} = P_i - P_j$ is defined as the pressure difference.

2.3. Free surface treatment

The kinematic free surface conditions can be automatically satisfied due to the mesh-free nature of SPH approach. The dynamic free surface conditions require a prescribed pressure to be imposed on the surface particles, such as $P = 0$. In the WCSPH computation the free surface particles do not need to be identified, since the pressure solution process is fully explicit, while this is needed in ISPH. In this paper, we use the three auxiliary functions combined with the ratio of particle number density to identify the free surface particles in an accurate way. More detailed implementation procedures can be referred to Zheng et al. (2014).

2.4. Mirror particle strategy

The mirror particles are used to reduce the boundary errors when we use the kernel approximation. This can also help to prevent the particles from penetrating the solid wall. The way to arrange the mirror particles and their implementation remain almost the same whether the boundary is moving or static. Here we use the standard mirror particle boundary by Liu et al. (2014) as the reference (named as ISPH_T for short) to compare with the improved boundary treatment in the subsequent sections.

2.5. Floating body algorithm

The floater's motion follows the Newton's laws as

$$[\boldsymbol{M}]\dot{\boldsymbol{U}}_c = \boldsymbol{F} \tag{16}$$

$$[\boldsymbol{I}]\dot{\boldsymbol{\Omega}} = \boldsymbol{N} \tag{17}$$

$$\frac{d\boldsymbol{S}}{dt} = \boldsymbol{U}_c \tag{18}$$

$$\frac{d\boldsymbol{\theta}}{dt} = \boldsymbol{\Omega} \tag{19}$$

where $\boldsymbol{F}$ and $\boldsymbol{N}$ are the force and moment actions on the floating body; $\boldsymbol{U}_c$ and $\dot{U}_c$ are the translational velocity and acceleration at the gravitational centre; $\boldsymbol{\Omega}$ and $\dot{\Omega}$ are the angular velocity and acceleration; $\boldsymbol{\theta}$ is the Eulerian angle; $\boldsymbol{S}$ is the translational displacement; and $[\boldsymbol{M}]$ and $[\boldsymbol{I}]$ are the mass and inertia matrices. Therefore, the velocity at a point on the floater is determined by

$$\boldsymbol{U} = \boldsymbol{U}_c + \boldsymbol{r}_b \times \boldsymbol{\Omega} \tag{20}$$

where $\mathbf{r}_b$ is the position vector to the gravitational centre.

In the SPH implementation, the following discretized equations are used for the force and moment calculations

$$\boldsymbol{F} = \sum_{k=1}^{n_s} \boldsymbol{n}_k P_{root,k} \Delta x_k \tag{21}$$

$$\boldsymbol{N} = \sum_{k=1}^{n_s} \boldsymbol{r}_{b,k} \times \boldsymbol{n}_k P_{root,k} \Delta x_k \tag{22}$$

where $P_{root,k} = P_k$ is the pressure of boundary particle; k is the segment ID; Δx_k is the initial particle spacing; $\boldsymbol{n}_k$ is the inner normal direction of Δx on the boundary segment k; n_s is the number of segments; and $\mathbf{r}_{b,k}$ is the vector length of Δx_k related to the centre of the object. The above pressure force and moment integration procedures on the solid boundary of the floater are shown in Fig. 1. Here it should be mentioned again that the pioneering work on wave–float interaction using the mesh-free particle modelling approach should be attributed to Koshizuka et al. (1998), where more details can be found there.

3. Improved solid boundary treatment

In this section, we start with a step-by-step improvement on the solid boundary treatment and propose the most accurate model for the wave–float interactions.

3.1. ISPH_TS scheme (SFDI used on pressure gradient only)

In the traditional ISPH calculation of the pressure gradient with the mirror particle approach, the computational results are heavily affected by the particle distributions and the shape of the solid boundary. To improve this, the first-order derivative of the pressure on the solid boundary was calculated by the Simplified Finite Difference Interpolation (SFDI) method originally by Sriram and Ma (2012) for their MLPG_R approach. SFDI is a second-order accurate numerical scheme based on the Taylor series expansions. In 2D case the key formulas of the pressure derivative are

$$\left(\frac{\partial P}{\partial x}\right)_{r_i} = \sum_{j=1,j\neq i}^{N} \frac{n_{i,x_m} B_{ij,x_k} - n_{i,xy} B_{ij,y}}{n_{i,x_1} n_{i,x_2} - n_{i,xy}^2} \left[P(r_j) - P(r_i)\right] \tag{23}$$

$$\left(\frac{\partial P}{\partial y}\right)_{r_i} = \sum_{j=1,j\neq i}^{N} \frac{n_{i,x_1} B_{ij,y} - n_{i,xy} B_{ij,x}}{n_{i,x_1} n_{i,x_2} - n_{i,xy}^2} \left[P(r_j) - P(r_i)\right] \tag{24}$$

$$n_{i,xy} = \sum_{j=1,j\neq i}^{N} \frac{(r_{j,x_m} - r_{i,x_m})(r_{j,xk} - r_{i,xk})}{|\mathbf{r}_j - \mathbf{r}_i|^2} W(|\mathbf{r}_j - \mathbf{r}_i|) \tag{25}$$

$$B_{ij,x_m} = \frac{(r_{j,x_m} - r_{i,x_m})}{|\mathbf{r}_j - \mathbf{r}_i|^2} W(|\mathbf{r}_j - \mathbf{r}_i|) \tag{26}$$

where $m = 1$ and $k = 2$ or $m = 2$ and $k = 1$ are used; N is the number of particles affecting the particle i; $x_1 = x$ and $x_2 = y$ are defined; and $r_{j,xm}$ is the component of position vector in x (or y) direction. Before applying the above equations to the solution of Eq. (11) in the next section, we first use them to replace Eq. (12) and then substitute into Eq. (6) to examine the numerical performance. This improved method is called ISPH_TS for short.

3.2. ISPH_BS scheme (SFDI modification of PPE on solid boundary)

In this section an idea of using the SFDI to treat the solid boundary during the solution of PPE is explored. The particles on the solid boundary should satisfy the pressure boundary condition, which is represented by the following momentum balance as

$$\mathbf{n} \cdot \nabla P = \rho(\mathbf{n} \cdot \mathbf{g} - \mathbf{n} \cdot \dot{\mathbf{U}}) \tag{27}$$

where $\boldsymbol{n}$ is the normal unit vector on the solid boundary. The above equation can be used to replace the standard PPE Eq. (10) on the solid boundary. The advantage of doing this is that the second-order pressure derivative is avoided and replaced by an exact first-order derivative, which can be more accurately calculated by the SPH particles even with disordered distributions. This should be able to maintain the pressure stability on the complex solid boundaries. By using the SFDI Eqs. (23–26), Eq. (27) can be rewritten as

$$n.\left\{ \sum_{j=1,j\neq i}^{N} \frac{n_{i,x_1} B_{ij,y} - n_{i,xy} B_{ij,x}}{n_{i,x_1} n_{i,x_2} - n_{i,xy}^2} \left[P(r_j) - P(r_i)\right] + \sum_{j=1,j\neq i}^{N} \frac{n_{i,x_m} B_{ij,x} - n_{i,xy} B_{ij,y}}{n_{i,x_1} n_{i,x_2} - n_{i,xy}^2} \left[P(r_j) - P(r_i)\right] \right\} = \rho(n \cdot g - n \cdot \dot{U}) \tag{28}$$

As shown above, the numerical approach that uses Eq. (28) to solve the pressure on the solid boundary rather than using Eq. (11) is named as ISPH_BS for short. By adopting this practice, there is no need to generate the mirror particles outside of the solid boundary. This makes the ISPH computations more efficient and accurate.

Here there are two issues that need to be clarified. For the ISPH_BS, there is no mirror (dummy) particle inside the

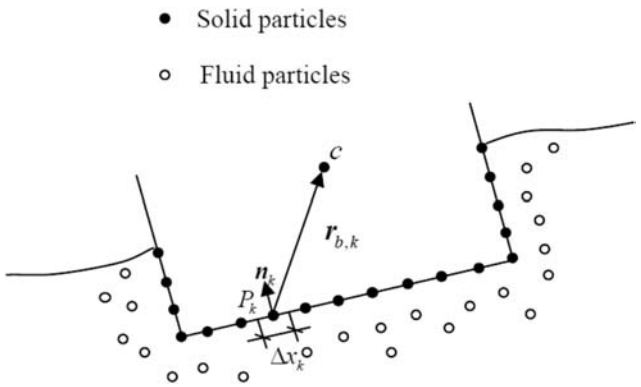

Fig. 1. Pressure force and moment integration procedure on the floater's boundary.

floating object. These dummy particles can help to calculate the particle density in WCSPH, but in ISPH the density keeps constant and the mass conservation is guaranteed by keeping the particle number, which is not changed in the computations. Therefore, there is no mass violation problem in the proposed ISPH_BS. In addition, it should be noted that the PPE in MLPG where the SFDI was originally adopted was discretized with an integration form while in ISPH it takes a partial differential form. However, this does not constitute an issue in the coupling of the two. Because SFDI is just one kind of the first-order derivative calculation methods, it can be easily adopted by similar numerical algorithms. A few background works on this have been documented to justify the compatibility between SFDI and SPH, such as by Zheng et al. (2014, 2017).

In summary, the key solution points of the improved SFDI boundary model (named ISPH_BS) are provided in Table 1. Besides, the proposed three ISPH models and their principles are summarized in Table 2.

3.3. Comparisons between ISPH_T and ISPH_TS

Now we set up two benchmark model tests to compare the modelling accuracy between ISPH_T and ISPH_TS as shown in Table 2.

The first test is about the static water contained in a rectangular pool, where the numerical length is $L = 1.0$ m and the water depth is $D = 0.4$ m. The origin of the coordinate system is placed on the left corner of the pool bottom. The total number of SPH particles used is 1440. The computational time step is 0.001 s and the total simulation time is 10 s. Fig. 2 shows the comparison of the computed time-dependent pressure gradient of the particle located at (0.5, 0.03) m, which is at the middle of the pool near the bottom boundary.

Table 2
Summary of three different ISPH numerical schemes.

Abbreviations	Boundary treatment	Equations used
ISPH_T	Mirror particles	Eq. (11) solved on inner and boundary particles; Eq. (12) used on inner particles
ISPH_TS	Mirror particles	Eq. (11) solved on inner and boundary particles; Eqs. (23–26) used on inner particles
ISPH_BS	No mirror particles	Eq. (11) solved on inner particles; Eq. (28) solved on boundary particles; Eqs. (23–26) used on inner particles

Since the water is in a hydrostatic state, the theoretical values of pressure gradient should be $\partial p/\partial x = 0$ and $\partial p/\partial y = -9.81$. By using 10,000 sampling points along the time axis in Fig. 2, the errors of ISPH_T are found to be 0.021 and 0.0073, respectively, for $\partial p/\partial x$ and $\partial p/\partial y$. In comparison, the errors are 0.0019 and 0.0014 only for the ISPH_TS computations.

The second test also involves the static water in the same water pool, but with a circular sphere being fixed on the free surface at the centre of the tank at (0.5, 0.4) m. The radius of the sphere is $R = 0.1$ m with a weight of 15.707 g. Consistent with the previous test case, the same spatial and temporal resolutions are used in the ISPH computations. Fig. 3 shows the comparison of computed time-dependent pressure gradient of the particle located at position coordinate (0.5, 0.283) m, which is slightly below the curve boundary of the sphere. Similar error analysis indicated that the errors of ISPH_T are 0.0482 and 0.0352, respectively, for the pressure gradient in x and y directions. In contrast, they are 0.0085 and 0.0024 for the ISPH_TS computations. This shows that ISPH_TS is more effective in reducing the numerical errors near the curved boundary, as compared with ISPH_T.

3.4. Comparisons between ISPH_TS and ISPH_BS for static problem

In this section, we use the same benchmark cases in Section 3.3 to compare the numerical performance between ISPH_TS and ISPH_BS, to find out the best scheme to calculate the pressure on the solid boundary.

For the first hydrostatic test, Fig. 4(a) shows the pressure distributions along the flow depth at the centre line of the tank, and Fig. 4(b) shows the time history of pressure at point (1, 0.05) m, which is located on the right tank wall at a distance of 0.05 m from the bottom. We find that although ISPH_TS can

Table 1
Key solution points of SFDI boundary model (ISPH_BS).

Particle type	Treatment method
Free surface	$P = 0$
Inner fluid	$\rho^* \sum_{j=1}^{N} m_j \frac{8}{(\rho_i+\rho_j)^2} \frac{P_{ij}\cdot \mathbf{r}_{ij}}{r_{ij}^2+\eta^2} \cdot \nabla_i W(\mathbf{r}_i - \mathbf{r}_j, h) = \alpha \frac{\rho-\rho^*}{\Delta t^2} + (\alpha - 1)\frac{\rho \nabla \cdot \mathbf{u}_*}{\Delta t}$
Solid wall	$\boldsymbol{n} \cdot \left\{ \sum_{j=1, j\neq i}^{N} \frac{n_{i,x_1} B_{ij,y} - n_{i,xy} B_{ij,x}}{n_{i,x_1} n_{i,x_2} - n_{i,xy}^2} [P(r_j) - P(r_i)] + \sum_{j=1, j\neq i}^{N} \frac{n_{i,x_m} B_{ij,x} - n_{i,xy} B_{ij,y}}{n_{i,x_1} n_{i,x_2} - n_{i,xy}^2} [P(r_j) - P(r_i)] \right\} = \rho(\boldsymbol{n}\cdot\boldsymbol{g} - \boldsymbol{n}\cdot\dot{\boldsymbol{U}})$

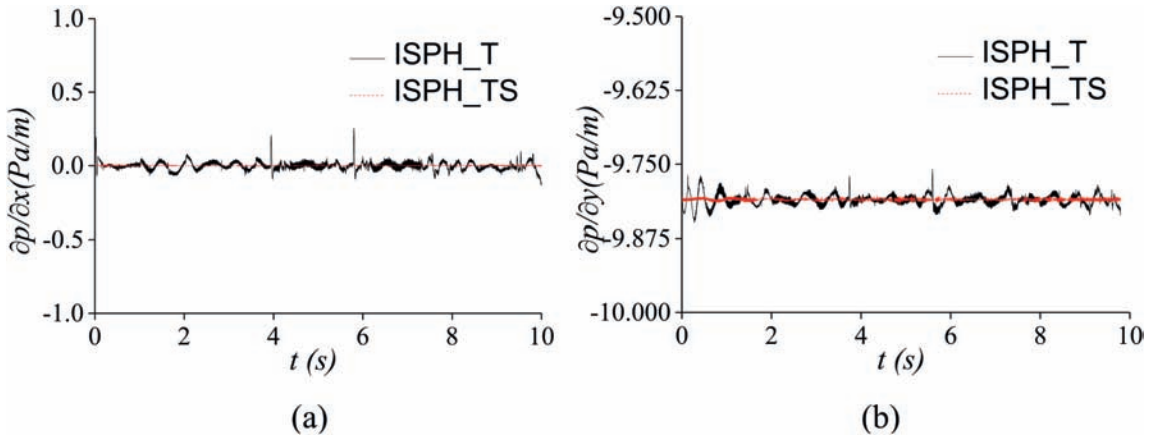

Fig. 2. Comparisons of time-dependent pressure gradient between ISPH_T and ISPH_TS for static water test: (a) $\partial p/\partial x$; and (b) $\partial p/\partial y$.

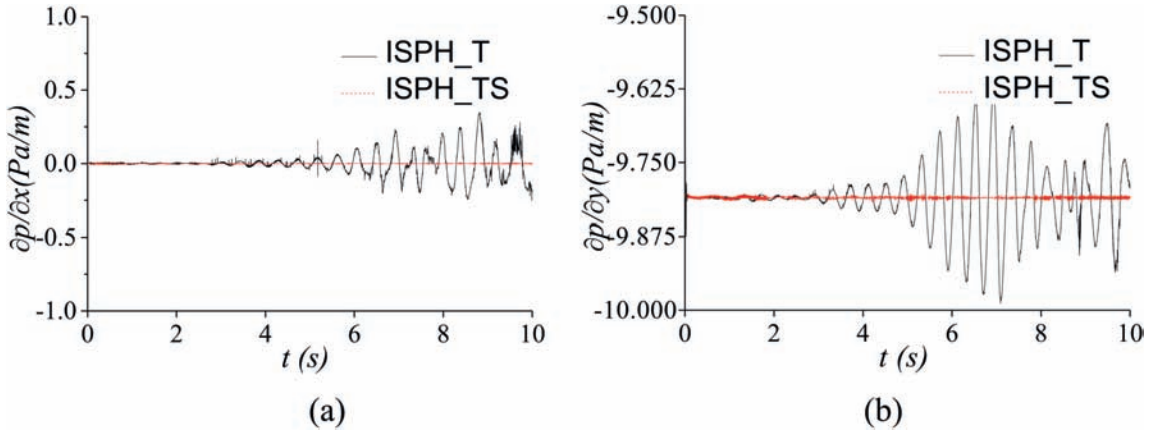

Fig. 3. Comparisons of time-dependent pressure gradient between ISPH_T and ISPH_TS for circular sphere fixed on static water surface: (a) $\partial p/\partial x$; and (b) $\partial p/\partial y$.

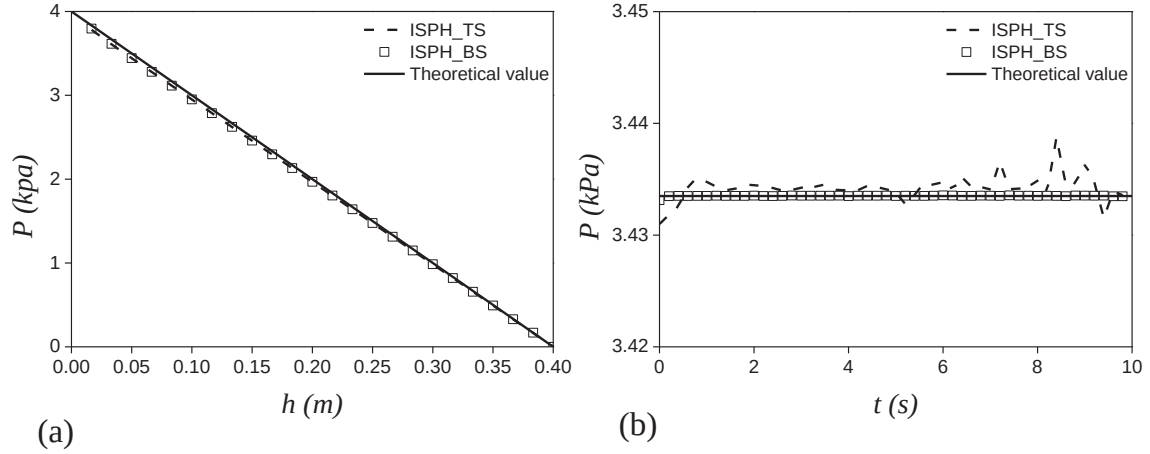

Fig. 4. (a) Pressure distribution along the flow depth. (b) Time history of pressure on right wall.

provide good pressure predictions away from the solid wall, the computed pressure on the boundary is not very accurate. In contrast, ISPH_BS computation shows the robustness due to the use of a higher-order SFDI scheme for the pressure solution. An analysis found that the numerical error of the ISPH_BS computations is only 1% of that of the ISPH_TS results and also the former saves the CPU time by around 25%.

For the next test on a circular sphere being fixed on the surface of still water, Fig. 5(a) and (b) shows the particle snapshot with pressure contour computed by the ISPH_TS and ISPH_BS, respectively. It indicates that the free surface particles near the

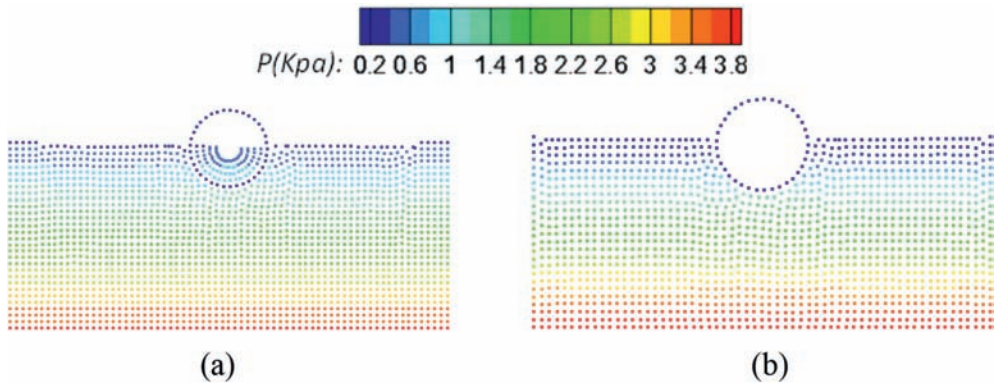

Fig. 5. Particle snapshot with pressure contour computed by (a) ISPH_TS; and (b) ISPH_BS.

curved boundary computed by ISPH_TS demonstrate some unstable patterns of clustering and gaping, while very orderly particle configurations are achieved by ISPH_BS. Fig. 6(a) shows the pressure distribution of the particles along the solid boundary of the sphere from point (0.5, 0.3) m to (0.6, 0.4) m, in which the pressure distributions calculated by ISPH_BS have a good agreement with the theoretical results, while the ISPH_TS computations demonstrate relatively large errors. Fig. 6(b) shows the time history of pressure computed at point (0.5, 0.3) m just on the lower curve boundary at the centre of the tank. Again the results show that the pressure calculated by ISPH_BS is much more stable and accurate than that calculated by ISPH_TS. For the numerical error and CPU efficiency, the ISPH_BS can reduce the error by 75% and save the CPU time by 20%. The reason for this is that the ISPH_TS method uses the mirror particles to treat the sphere boundary, and the mirror particles are difficult to arrange due to the boundary curvature. Therefore, the spacing of mirror particles becomes smaller than the inner particle spacing Δx and their densities increase accordingly. Since ISPH_TS uses Eq. (11) to solve the pressure on the boundary as well, the value of $\nabla \cdot \mathbf{u}_*$ is strongly influenced by the mirror particles near the curve boundary and the accuracy of boundary pressure calculations is degraded. On the other hand, ISPH_BS method uses Eq. (28) to solve the boundary particle pressure, so it is free of using the mirror particles. Besides, it uses the high-accuracy SFDI scheme to calculate the pressure of particles. These have also reduced the kernel truncation effect on the solid boundary.

Here some additional discussions are needed to explain the particle distribution issues near the curved sphere boundary. First it should be noted that the measures of kernel function could also play an important role in this according to the study of Oger et al. (2007). Secondly, the unified semi-analytical boundary as proposed by Leroy et al. (2014) could also effectively improve the complex solid boundary treatment, although its numerical accuracy was found to be slightly lower than the present SFDI scheme used in ISPH_BS. Finally, the issue with difficulties in placing the ghost particles near the curved boundaries has been researched significantly. For WCSPH, the following benchmark works have been documented, such as the mirror particles of Takeda et al. (1994), fixed ghost particles of Marrone et al. (2011, 2013), and mirror particles with the local force balance of Adami et al. (2012). For ISPH, there are widely adopted multiple boundary tangent technique (MBTT) of Yildiz et al. (2009) and Shadloo et al. (2011). Most of these works deal with the WCSPH modelling approach while the solid boundary treatment is quite different in ISPH especially when solving the PPE with a free surface boundary. The ISPH based MBTT has been tested on relatively simple geometries but not easily applicable to more complex ship or aircraft boundaries. In this sense, the proposed SFDI used in ISPH_BS provides an accurate scheme to

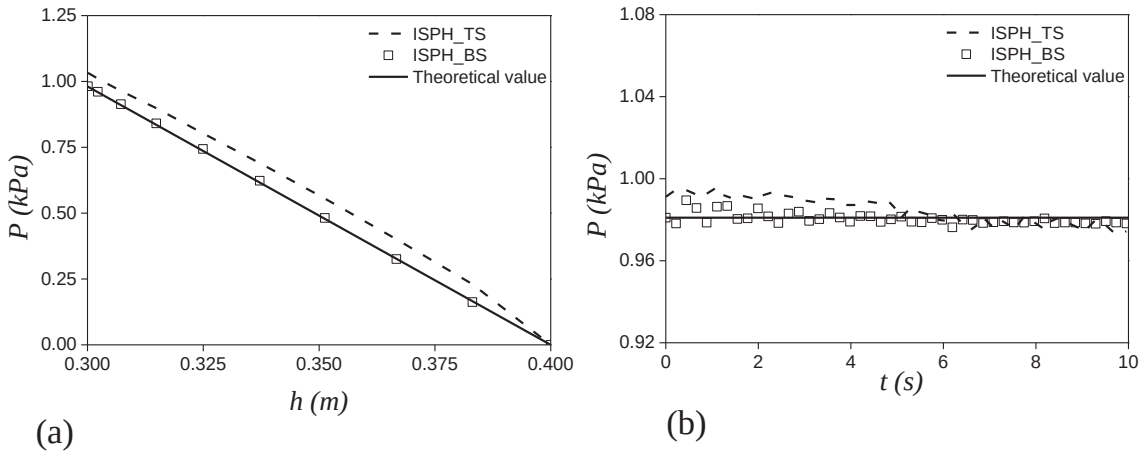

Fig. 6. (a) Pressure distribution along the flow depth on right of sphere. (b) Time history of pressure on lower sphere boundary.

be coupled with the ISPH solver. It is much more straightforward and also mirror particle free on the solid boundary. Therefore, more accurate implementation of the pressure boundary condition is achievable.

To conclude the static test and further explore the numerical performance of ISPH_TS and ISPH_BS, a mini-tank is used with $L = 1.0$ m long and the water depth $D = 0.4$ m, with the coordinate origin being located on the left corner of the tank bottom. To examine the pressure calculations near the solid boundary, we consider pressure $P_{i,b}$ at the middle of tank bottom, and $P_{i+1,f}$, which is the pressure of an inner fluid particle just above the location of $P_{i,b}$ at a distance of Δy, as shown in Fig. 7(a) or (b). In ISPH_TS approach as illustrated in Fig. 7(a), the pressure of solid boundary particle $P_{i,b}$ is solved by Eq. (11), and the ghost particles are added to satisfy the pressure gradient condition at the solid boundary by $\frac{\partial P}{\partial x}n_x + \frac{\partial P}{\partial y}n_y = \rho(n\cdot g - n\cdot \dot{U})$. Under the hydrostatic state with only the influence of gravity, this condition can be simplified as $P_b - P_g = -\rho \boldsymbol{g}(y_b - y_g)$, where P_b and P_g are the pressure of solid boundary and ghost particles, respectively. The kernel support domain of Eq. (11) used by the ISPH_TS is $2.0\Delta x$, so two layers of the ghost particles are added as shown in Fig. 7(a). In this sense, the ghost particles contribute to the boundary condition, while the nearby fluid particles are solved by Eq. (11). On the other hand, as shown in Fig. 7(b), the solid boundary particles are solved by Eq. (28) in the ISPH_BS using SFDI without the need of any ghost particles. To maintain the high accuracy of the SFDI scheme, the kernel support domain near the solid boundary is expanded to $4.0\Delta x$. To show the improvement of ISPH_BS over ISPH_TS, the pressure difference of $P_{i,b} - P_{i+1,f}$ is monitored with the time. By using a vertical particle spacing of $\Delta y = 1/60$ m, Fig. 7(c) gives the comparison of pressure time history of $P_{i,b} - P_{i+1,f}$ computed by ISPH_TS and ISPH_BS, along with the analytical value of 0.16 KPa obtained from the hydrostatic law. Again, it shows that the pressure calculations on the solid boundary are well predicted by ISPH_BS, while relatively large errors are found in ISPH_TS.

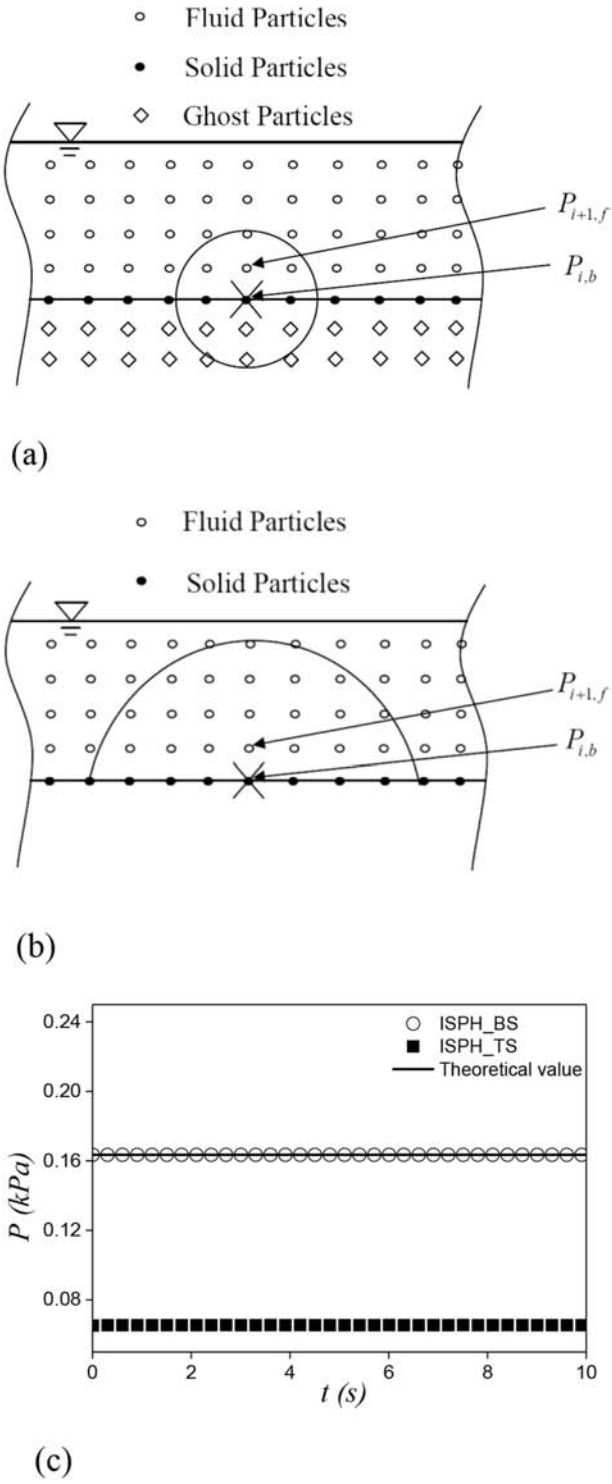

Fig. 7. Solid boundary treatment and pressure calculations for ISPH_TS and ISPH_BS. (a) Solid boundary treatment in ISPH_TS. (b) Solid boundary treatment in ISPH_BS. (c) Pressure time history of $P_{i,b}$–$P_{i+1,f}$.

3.5. Comparisons between ISPH_TS and ISPH_BS for dynamic problem

To examine the superiority of ISPH_BS in solving the pressure of moving solid boundary, another test case is used as shown in Fig. 8, in which a floating box is initially placed on the still water surface. The length of the water tank is $L = 3$ m and the flow depth is $D = 0.4$ m. The floating box is homogeneous and its centre is fixed at point (1.5, 0.4) m. The initial angle of the

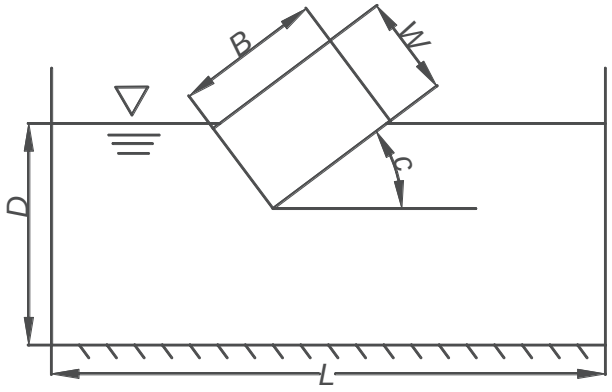

Fig. 8. Floating object on water surface with an inclination angle.

inclination is $C = -11.5°$ (counter-clockwise is defined as being positive). The dimension of the box is $W = 0.2$ m and $B = 0.3$ m, and the density of the box is equal to that of the water. The ISPH computational particle spacing is $\Delta x = 0.005$ m. After the release of the floating box from its original position, it starts to oscillate under the action of the gravity and eventually stabilizes at a balanced position due to the viscous dissipation. Both ISPH_TS and ISPH_BS methods are used to calculate the rolling process and the angle variations are compared with the experimental data (Ren et al., 2015).

Fig. 9 shows the time history of rolling angle computed by ISPH_TS and ISPH_BS, which again shows the latter is more accurate since it provides much better agreement with the experiment data on the time-dependent rolling process. The mean error between the ISPH_BS computations and experimental data is 0.0154, as compared with 0.0264 for the ISPH_TS. As the rolling angle of the object is associated with the pressure on the boundary, it implies ISPH_BS is more promising in dealing with the moving boundary as well.

To investigate the convergence of the model, additional two particle spacings are used to run the same case, i.e. $\Delta x = 0.01$ m and 0.02 m, as compared with the original $\Delta x = 0.005$ m. The time histories of rolling angle are shown in Fig. 10(a) and (b), respectively, for the ISPH_BS and ISPH_TS computations. It can be seen that the computation made with $\Delta x = 0.005$ m has the best agreement with the experimental data for both models. Besides, ISPH_BS demonstrates much more promising convergence behaviour than the ISPH_TS, since the former achieved better match with the experimental data even with particle size $\Delta x = 0.01$ m. The robustness of ISPH_BS can be further supported by the error analysis as shown in Fig. 11, where the relationship between the numerical errors and particle numbers is plotted on a logarithmic scale. The error of roll motion can be determined by $Err = |\sum_{i=1}^{ncal} f_i(t_i - t_{i-1}) - \sum_{k=1}^{nexp} f_k(t_k - t_{k-1})|/|\sum_{k=1}^{nexp} f_k(t_k - t_{k-1})|$, where f is the value of roll motion, *ncal* is the

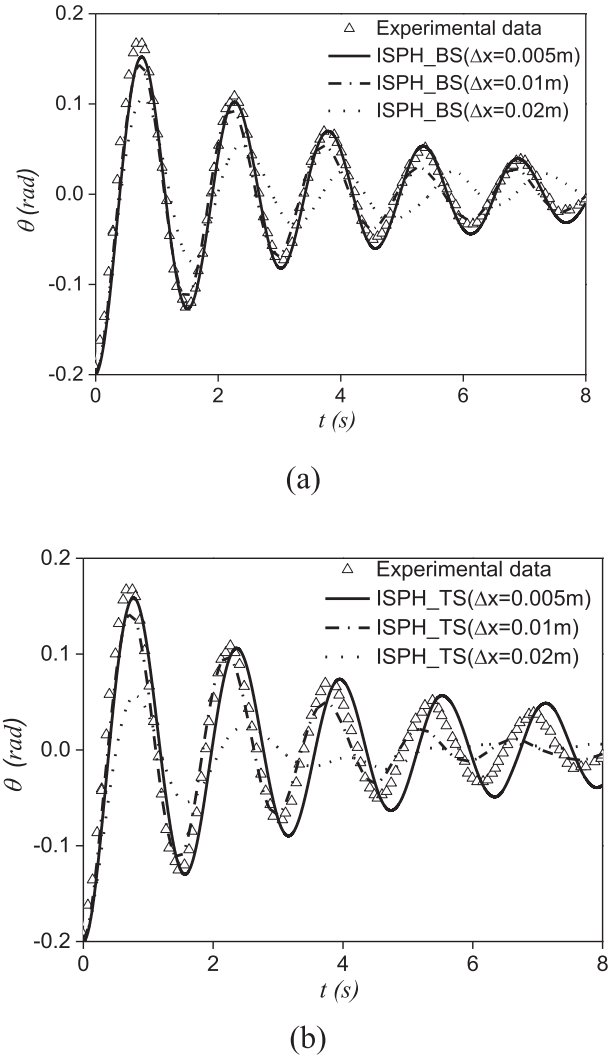

Fig. 10. Time history of rolling angles computed with three different particle spacings by using (a) ISPH_BS; and (b) ISPH_TS.

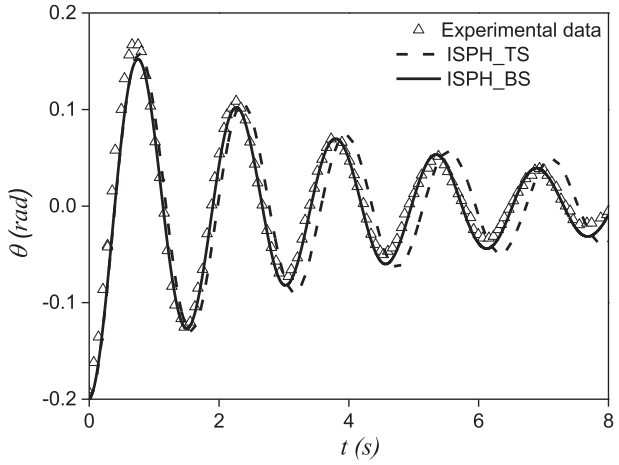

Fig. 9. Time history of rolling angle computed by ISPH_TS and ISPH_BS, compared with experimental data of Ren et al. (2015).

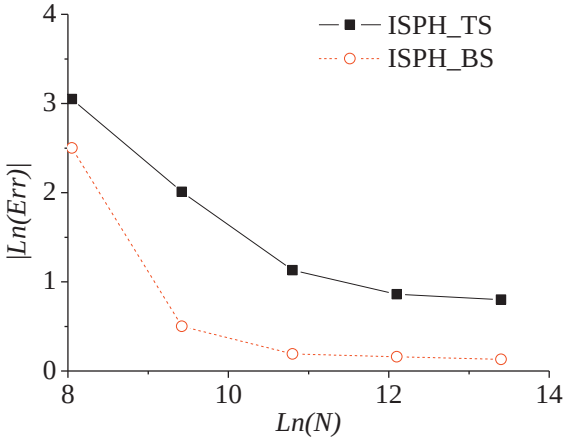

Fig. 11. Relationship of numerical error with particle number for two ISPH schemes.

result number of calculation, *n*exp is the result number of experimental data.

However, it should be cautioned that the adoption of SFDI in SPH could make the study on convergence highly complex and thus the convergence should be examined with respect to the smoothing length as well, apart from the particle spacing. For this purpose we study different kernel smoothing lengths and test their influence on the simulation results, by using $h = 0.6-1.6\Delta x$ for ISPH_BS only. The results are shown in Fig. 12(a) for the time history of rolling angles of the float and Fig. 12(b) for the numerical errors with the smoothing length. It is found that the best performance happens around where $h = 1.0\Delta x$ and the numerical errors increase towards either very small or very large h. More in-depth studies on the smoothing length convergence can be found in Quinlan et al. (2006).

Although SFDI is a highly accurate first-order derivative calculation method, its accuracy near the solid boundary under non-uniform particle distributions is more or less around first-order level, according to the latest research by Zheng et al. (2017). In this sense, SFDI could be regarded to have the same rate of convergence as the other SPH approximation methods so a direct comparison can be made for the ISPH_BS. Here an accuracy study on the different ghost/mirror particle techniques as found in Macia et al. (2011) is made, and compared with the SFDI in ISPH_BS. The test involves the particles being arranged in a square domain of 1.0 m by 1.0 m with uniform particle distributions.

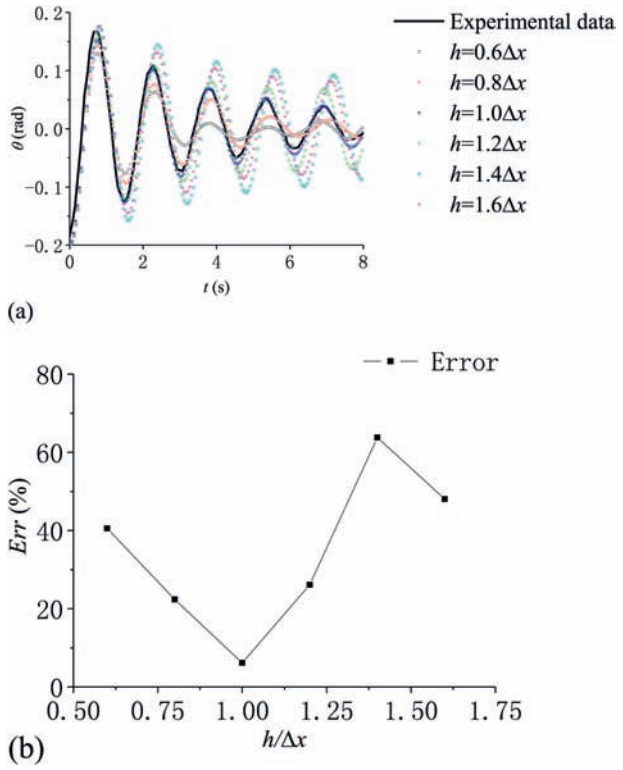

Fig. 12. (a) Time history of rolling angles computed with different kernel smoothing lengths by ISPH_BS. (b) Relationship of numerical error with smoothing length for ISPH_BS.

Different particle sizes Δx are used, i.e. 0.02 m, 0.01667 m, 0.0125 m, 0.01 m, 0.0083 m and 0.00667 m, respectively. For an analytical function $f = \exp(x + y)$, consider a location on the centre of the bottom boundary at $(x,y) = (0.5, 0.0)$ and calculate $\partial f/\partial x$ by using four mirroring models in Macia et al. (2011) and SFDI for the alternative particle sizes. Fig. 13 gives the convergence test of errors with Δx for different boundary treatment methods, where SFDI once again shows the most promising performance.

To conclude the dynamic test and finally explore the numerical performance of ISPH_TS and ISPH_BS, a benchmark test of moving body application is carried out to check the pressure calculations near the solid boundary. The dimension of the mini-tank is of the length $L = 1.0$ m and water depth $D = 0.4$ m. There is a square box initially situated on the free water surface with side length $L_b = 0.2$ m, and its gravity centre is just on the surface line. The box is subjected to a forced motion in the vertical direction described by $y = \varphi\sin(\omega t)$, where $\omega = \sqrt{g/(2D)}$ is defined. So the vertical acceleration of the box can be determined by $a_y = -\varphi^2\omega\sin(\omega t)$. A schematic diagram of the mini-tank and the moving box is shown in Fig. 14(a).

By considering the gravity effect only, the pressure difference between the solid boundary particle on the mid-bottom of the moving box and the downward fluid particle is calculated by $P_{i,b} - P_{i-1,f} = \rho g\Delta y + a_y$, where $P_{i-1,f}$ indicates the location just under the centre of the box bottom with a prescribed distance of $\Delta y = 1/60$ m. Since the position of $P_{i-1,f}$ always changes following the box motion, the pressure value of $P_{i-1,f}$ can only be determined by using the kernel approximation. Fig. 14(b) gives the comparisons of time history of pressure $P_{i,b}-P_{i-1,f}$ for the forced motion computed by ISPH_TS and ISPH_BS. Although both numerical results demonstrate some kinds of error when comparing with the theoretical values calculated by $P_{i,b} - P_{i-1,f} = \rho g\Delta y - \phi^2\omega\sin(\omega t)$, ISPH_BS achieved much more favourable results.

Since extensive comparisons have been made on the different ISPH solution schemes, in the next two sections of the model application, only the most promising ISPH_BS model is used for the computations.

4. Model validations in wave-structure interactions

4.1. Wave interaction with a fixed structure

The computation in this section is based on the study of Ren et al. (2015). The numerical wave tank is 10 m long and 1.8 m high with the water depth of 1.2 m. A fixed rectangular box is placed on the water surface and partially immersed, with the centroid being located at point (4.6 m, 1.2 m). The length of the box is 0.8 m and the height is 0.4 m. The numerical damping zone is set from a distance of 3 m away from the right boundary to absorb the outgoing waves. A schematic setup of the numerical wave flume is shown in Fig. 15.

In the ISPH model setup, there are 19,200 fluid particles and 514 boundary particles. Two wave conditions are

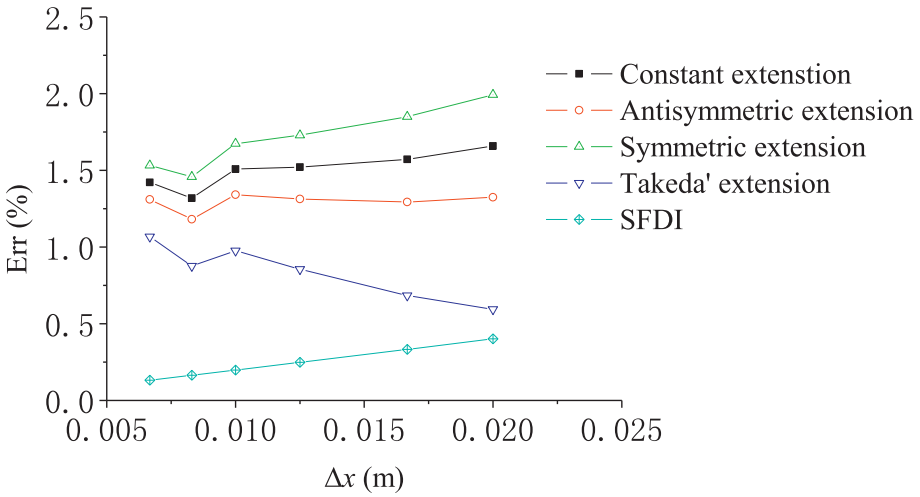

Fig. 13. Convergence test of errors with Δx for different mirroring models in Macia et al. (2011) and SFDI near solid boundary.

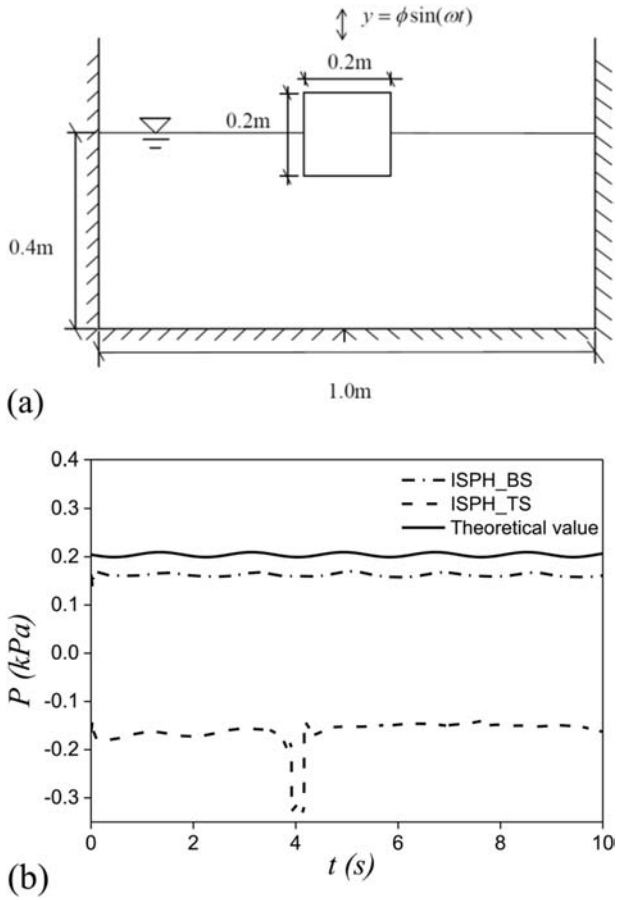

Fig. 14. (a) Schematic diagram of mini-tank and moving box with forced motion. (b) Time history of pressure $P_{i,b}-P_{i-1,f}$ computed by ISPH_TS and ISPH_BS for forced box motion.

considered: in the first condition the wave height is $H = 0.06$ m and wave period is $T = 1.2$ s. In this case the wave can be considered as a linear wave; in the second condition, the wave period keeps the same but the wave height increases to $H = 0.2$. In this case the relative wave height reaches 0.089 so the linear wave theory does not hold. The ISPH_BS model is used to calculate the horizontal wave force (F_x), vertical wave force (F_y) and overturning moment (M). These are compared with the dynamic boundary particles SPH (DBPs_SPH) results (Ren et al., 2015) based on the WCSPH and the analytical results using the frequency domain analysis (Mei and Black, 1969). The ISPH_BS computational results are shown in Figs. 16–18 for the three different wave loading parameters. It shows that a very satisfactory agreement has been found in the linear waves, while larger discrepancies appear in the nonlinear ones.

To quantify the accuracy of ISPH_BS model, only the linear wave results are analyzed because the analytical results in nonlinear waves are not sufficiently accurate. Here the mean error is evaluated between the ISPH_BS and analytical results, and compared with the error of DBPs_SPH results of Ren et al. (2015). It has been found that both numerical results could achieve satisfactory match with the analytical ones of Mei and Black (1969), but the ISPH_BS predicted four-time smaller error than the DBPs_SPH in the vertical forces and overturning moments. On the other hand, while calculating the horizontal forces the DBPs_SPH computations achieved twice smaller error. However, considering the fact that ISPH_BS used a particle size of 0.02 m as compared with 0.01 m used by DBPs_SPH, the present model seems to be quite promising.

4.2. Wave interaction with a floating structure

In this section we consider the wave interaction with a floating structure, by following the experimental and numerical works of Ren et al. (2015). The general layout of the numerical wave tank is the same as shown in Fig. 15, except that the depth of water is changed to 0.4 m and the rectangular object is allowed to move. The length of the movable box is 0.3 m and its height is 0.2 m. The initial position of the centroid of the box is placed at (2.0 m, 0.4 m) and the box can have the swaying, heaving and rolling motions with three-degree freedom. Following Ren et al. (2015), the following

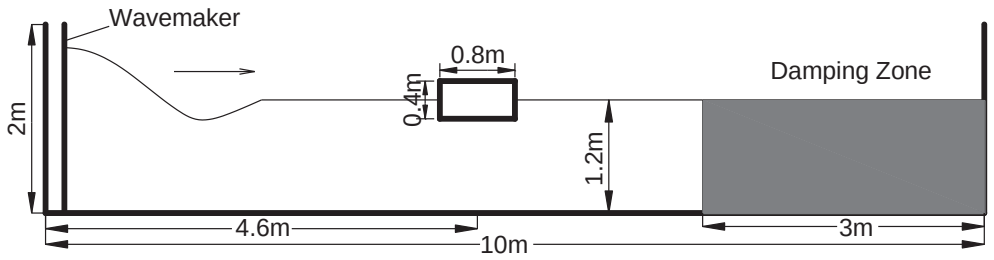

Fig. 15. Numerical wave flume for wave interaction with a fixed structure.

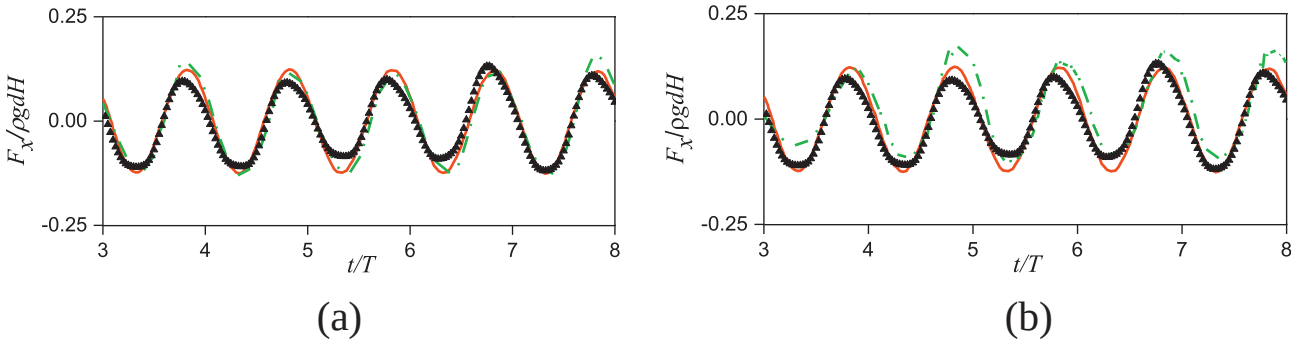

Fig. 16. Horizontal force: (a) linear wave; and (b) nonlinear wave (Red: analytical results of Mei & Black; Green: WCSPH of Ren et al.; Black: ISPH_BS).

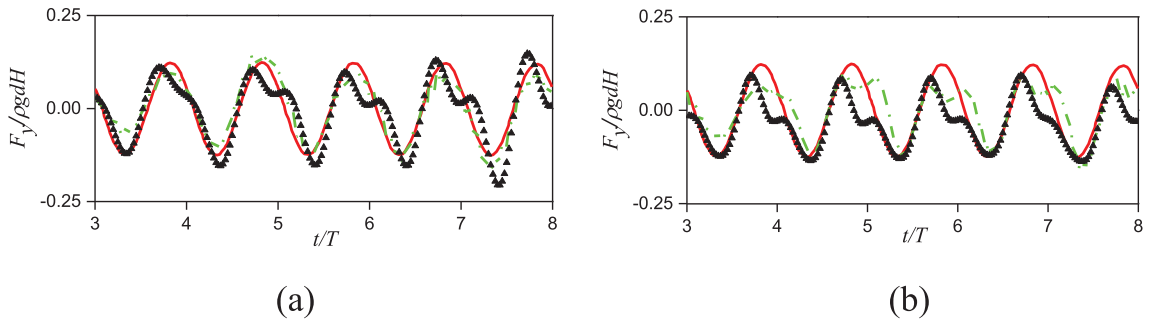

Fig. 17. Vertical force: (a) linear wave; and (b) nonlinear wave (Red: analytical results of Mei & Black; Green: WCSPH of Ren et al.; Black: ISPH_BS).

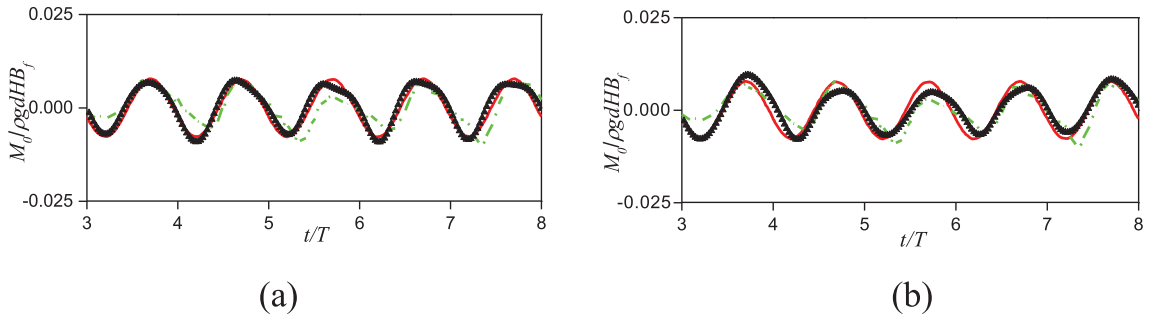

Fig. 18. Overturning moment: (a) linear wave; and (b) nonlinear wave (Red: analytical results of Mei & Black; Green: WCSPH of Ren et al.; Black: ISPH_BS).

two wave conditions are examined: $H = 0.04$ m with $T = 1.2$ s; and $H = 0.1$ m with $T = 1.2$ s. The former corresponds to a linear wave while the latter demonstrates strong nonlinear feature. The computational particle size is taken as $\Delta x = 0.005$ m in all the ISPH_BS computations. Figs. 19–21 show the time histories of different motion modes of the floating box under two wave conditions. Meanwhile, the experimental data and DBPs_SPH results (WCSPH) of Ren et al. (2015) are shown for a comparison. Generally it shows the ISPH_BS computations achieve better agreement with the experimental data as compared with the DBPs_SPH results, especially for the larger amplitude waves.

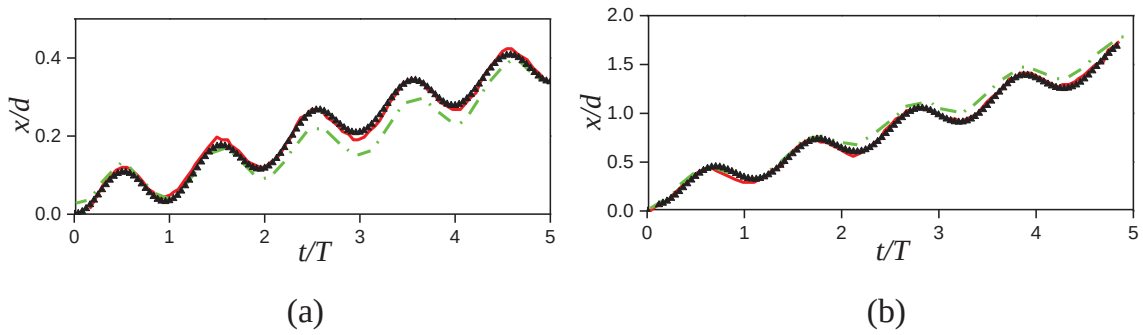

Fig. 19. Swaying motion: (a) linear wave; and (b) nonlinear wave (Red: experimental data; Green: WCSPH of Ren et al.; Black: ISPH_BS).

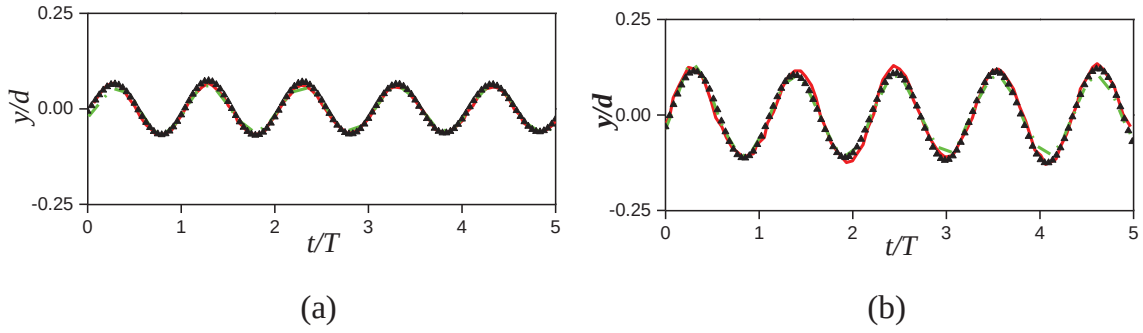

Fig. 20. Heaving motion: (a) linear wave; and (b) nonlinear wave (Red: experimental data; Green: WCSPH of Ren et al.; Black: ISPH_BS).

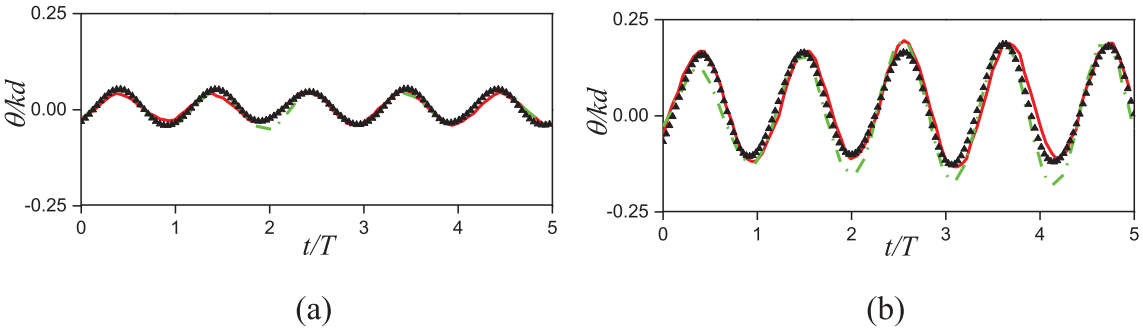

Fig. 21. Rolling motion: (a) linear wave; and (b) nonlinear wave (Red: experimental data; Green: WCSPH of Ren et al.; Black: ISPH_BS).

The mean errors between the numerical results and experimental data are shown in Table 3 for the two wave conditions, three structure motion modes and two SPH computations. Once again it proves that the results calculated by ISPH_BS are much more encouraging than those calculated by DBPs_SPH for either the linear or nonlinear wave conditions.

Table 3
Mean errors between numerical results and experimental data.

	Linear wave		Nonlinear wave	
	DBPs_SPH	ISPH_BS	DBPs_SPH	ISPH_BS
Swaying motion	2.93e-04	1.52e-04	4.65e-04	1.49e-04
Heaving motion	6.82e-04	6.79e-04	9.92e-05	6.65e-05
Rolling motion	5.55e-04	3.21e-04	1.55e-04	1.17e-04

For illustration, Fig. 22 shows the float motion under the wave within one wave period. The ISPH_BS computations (left) are compared with the experimental photos (right, Ren et al., 2015) for the larger wave height, i.e. $H = 0.1$ m and wave period $T = 1.2$ s. A satisfactory agreement with the experiment on the wave shape and float movement is demonstrated at each time instant.

5. Green water impact on a floating deck

Severe marine environment could generate the green water and lead to the intense rocking motion of the ships. Strong impact loads from the green water could bring tremendous damages to the deck equipment and the superstructure, which influence the safe navigation. The conventional grid models are insufficient to reproduce the entire process of green water

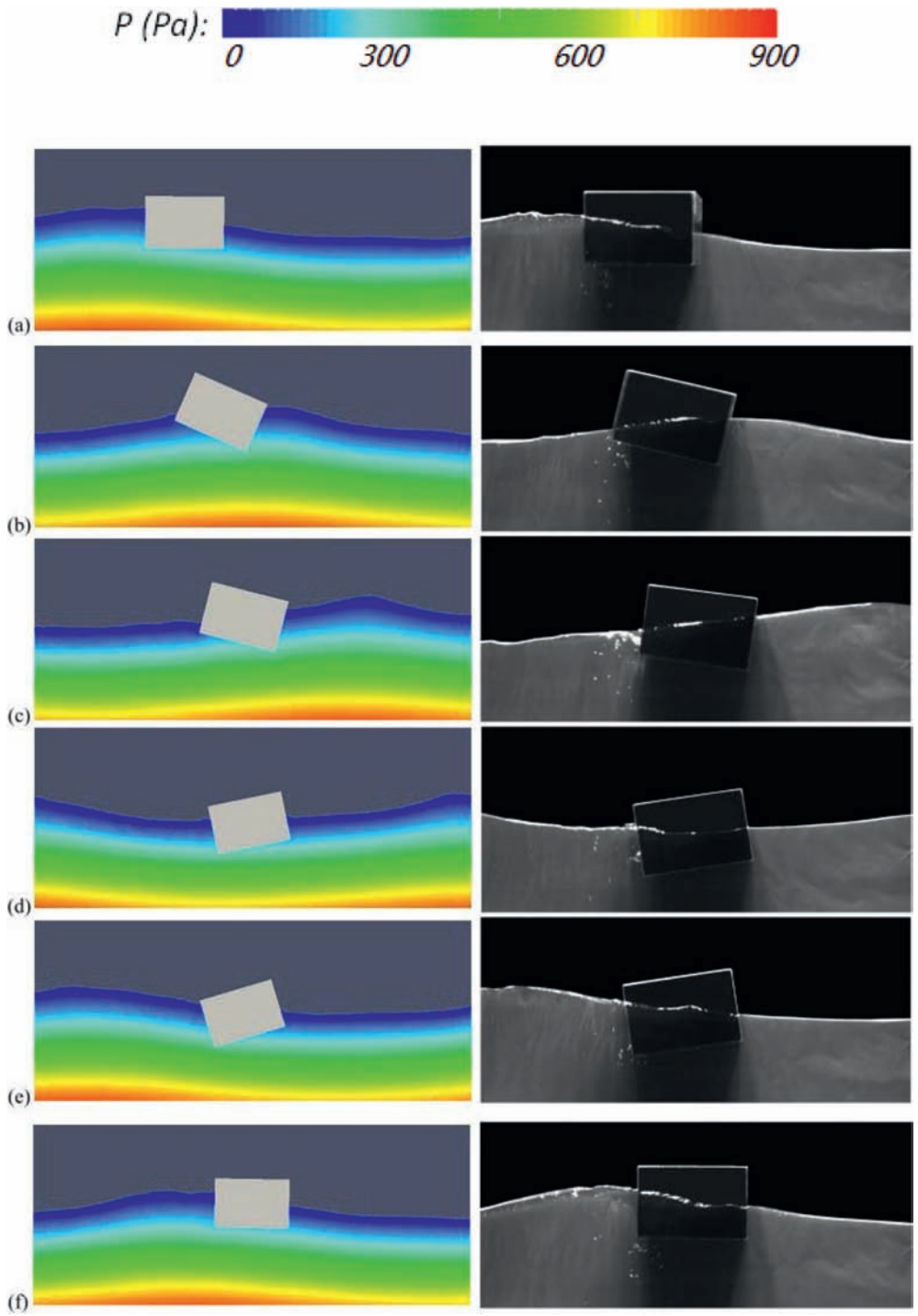

Fig. 22. Float motion under the wave computed by ISPH_BS (left), compared with the experimental photos (right) at time: (a) $t = t_0$; (b) $t = t_0 + T/4$; (c) $t = t_0 + T/2$; (d) $t = t_0 + 3T/4$; (e) $t = t_0 + T$; and (f) $t = t_0 + 1.09T$.

overtopping due to the nonlinear wave surface deformation and breaking. Since the proposed ISPH_BS method has the advantage in capturing the free surface and solving the pressure on the solid boundary, it is used in this section to simulate the green water impact on a 2D deck. To complement the numerical work, a physical experiment has been carried out in Harbin Engineering University. Measurements on the water surface, impact pressure and motion trajectory of the floating object has been taken.

5.1. Physical experiment

The test used a ship-shape as the object, to visualize the green water overtopping and impact on the deck in a practical sense. The physical model is a simplified version, and the main body is made of the glass fibre reinforced plastic. It is a box type of the floating structure, and the upper layer of the deck is also a rectangular structure. In order to generate sufficient overtopping, the test model is designed with a low

Table 4
Basic parameters of the physical model.

Parameters	Symbols	Values
Length	L	0.7 m
Width	B	0.5 m
Waterline	T	0.25 m
Displacement of water	Δ	89.25 kg
Initial stability height	G_M	0.06834 m
High center of gravity	Z_g	0.13171 m
Rolling period	T_r	1.20 s
Heaving period	T_h	1.15 s
Moment of inertia	I	4.5717 kg m^2

freeboard. The basic parameters of the deck model are given in Table 4. The schematic view is shown in Fig. 23(a) and (b) shows the locations of pressure measurement during the experiment. One pressure sensor is used to measure the pressure of inside deck and this is installed on the deck 0.05 m away from the upper vertical plate. Another sensor is installed on the waterline position.

The physical model test is carried out in a 30 m long, 0.8 m wide and 1.0 m high wave flume. The initial water depth is 0.7 m. The flume is equipped with a single board push–pull wave machine that can generate the wave height of 0.02–0.25 m and wave period of 0.5–5.0 s. Both the regular and random waves with a wide range of spectrums can be generated for the study purpose. Wave energy dissipation device is installed at the other end of the wave tank. The experimental wave flume with the floating deck is shown in Fig. 24. Laboratory measurements include the heaving, swaying and rolling motions as well as the wave impact pressure on key locations of the model. Experimental high-quality videos are also processed to visualize the dynamic process of wave interactions with the floating deck.

5.2. ISPH computational parameters

In the ISPH_BS computations, the regular wave experiment is reproduced. Four different wave periods, which are 1.0 s, 1.2 s, 1.5 s and 2.0 s; and two different wave heights, which are 0.05 m and 0.1 m, have been simulated and compared with the experimental measurements. The length of the numerical

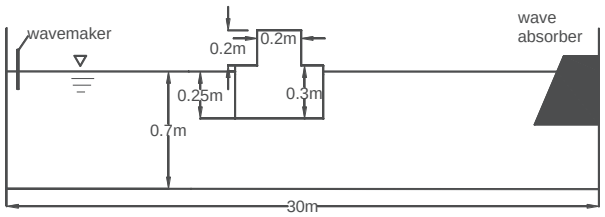

Fig. 24. Experimental wave flume and the floating deck.

tank is 30 m and the initial depth of water is 0.7 m. The total particle number is 210,000 and the initial particle spacing is 0.01 m. The computational time step is 0.001 s and the total simulation time is 40 s. The simulations are performed on a workstation using an Intel Core i7-7700 K Processor (8 M Cache, 4.2 GHz, 8.0 GT/s) and 32G RAM under a WIN 7 (64-Bit Edition) operating system.

5.3. Results and discussions

By ISPH_BS computation, the particle snapshots and the motion of the floating deck during the green water attack are shown in Fig. 25(a–d) within one wave period. The numerical results are based on the wave height $H = 0.1$ m and wave period $T = 1.0$ s. It shows that both the wave surface deformations and float movement have been well captured by the ISPH_BS computations. When the wave approaches to the float, it orientates to the offshore direction as shown in Fig. 25(a); when the severe wave impact occurs, it tilts to the onshore direction as shown in Fig. 25(c). The returning flow from the deck to the sea is also well reproduced by the numerical simulations as shown in Fig. 25(d).

To quantify the accuracy of ISPH_BS model in predicting the wave impact pressures and the float motion, Figs. 26 and 27(a) and (b) provide the time history of the wave impact pressures inside the deck and on the waterline for the two different wave conditions ($H = 0.05$ m and $t = 1.0$ s, representing a smaller amplitude linear wave; $H = 0.1$ m and $t = 1.0$ s, representing a larger amplitude nonlinear wave), respectively. Besides, Fig. 28 provides the time history of the heaving motion of the floating deck. It can be seen that the

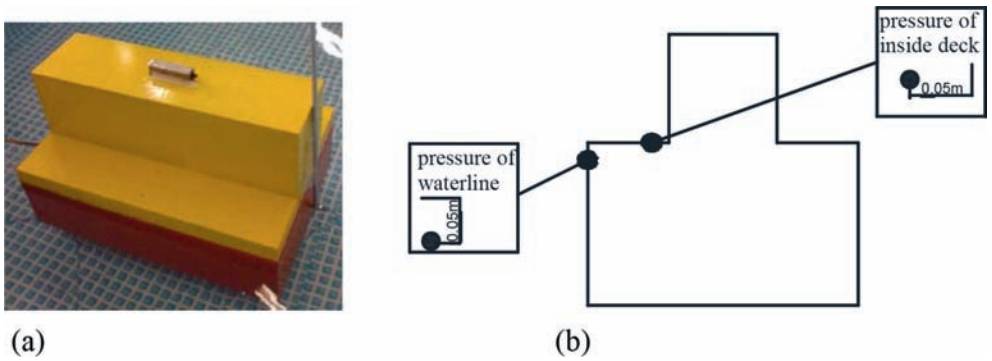

Fig. 23. (a) Schematic view of test model. (b) Pressure sensors on the model.

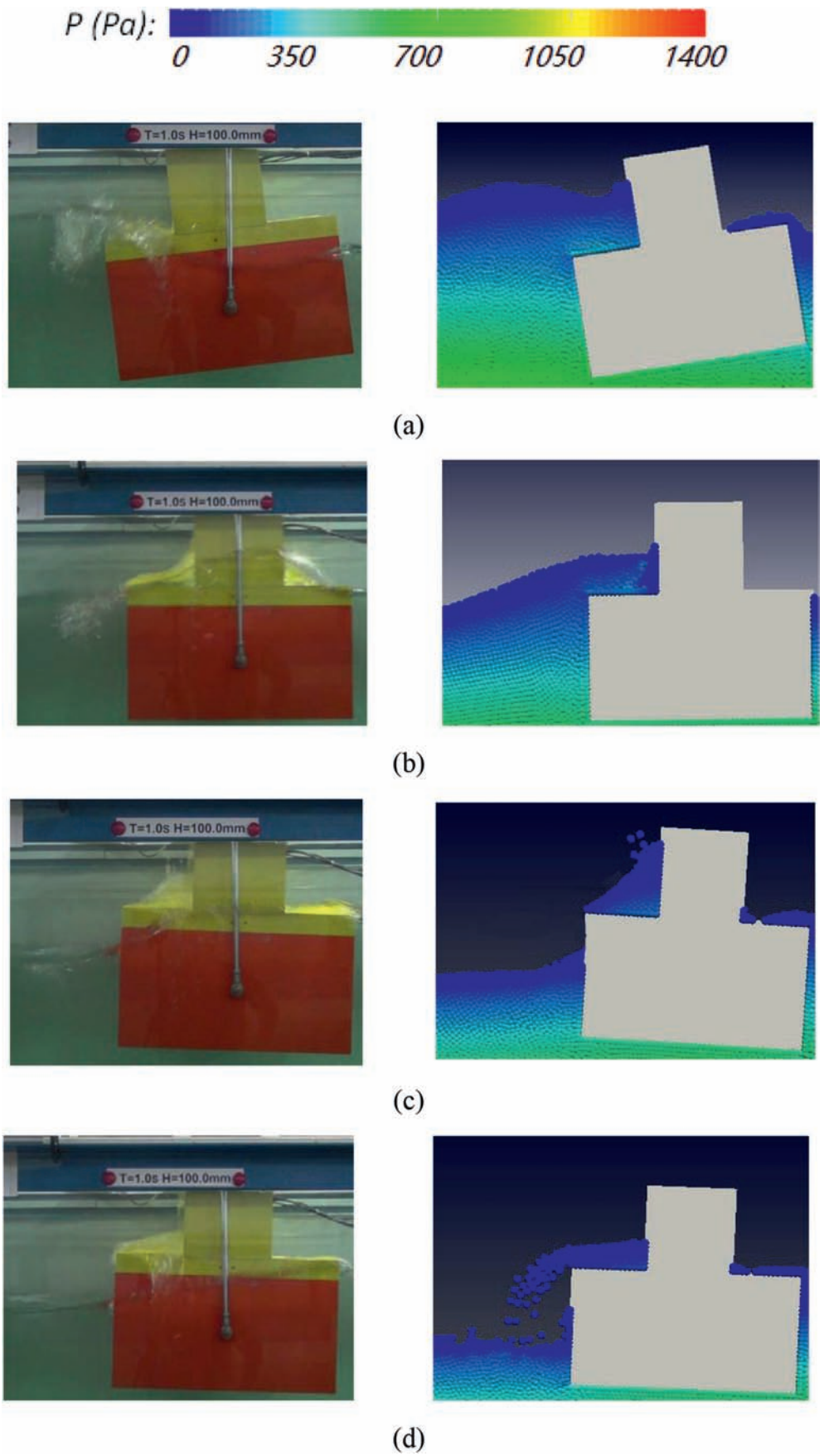

Fig. 25. Particle snapshot and float movement during green water attack, compared between experimental photos (left) and ISPH computations (right) at time: (a) $t = t_0$; (b) $t = t_0 + T/4$; (c) $t = t_0 + T/2$; and (d) $t = t_0 + 3T/4$.

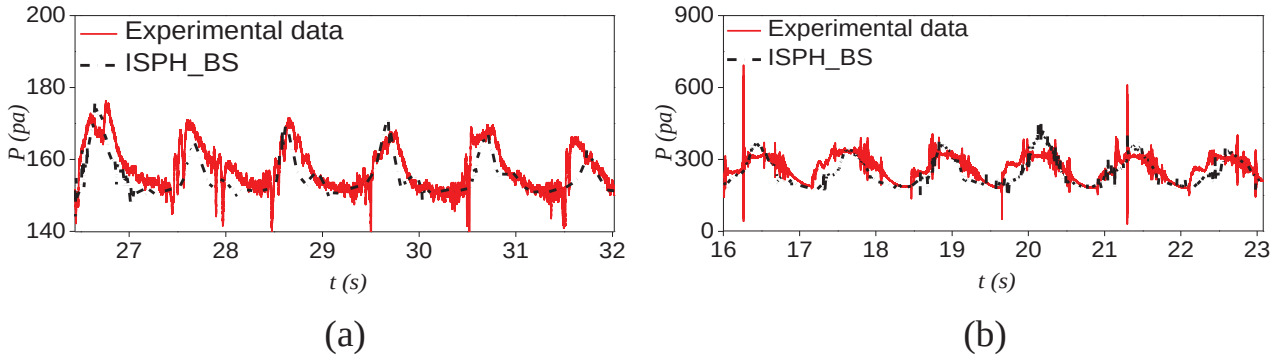

Fig. 26. Time history of impact pressure inside deck: (a) smaller amplitude wave; and (b) larger amplitude wave.

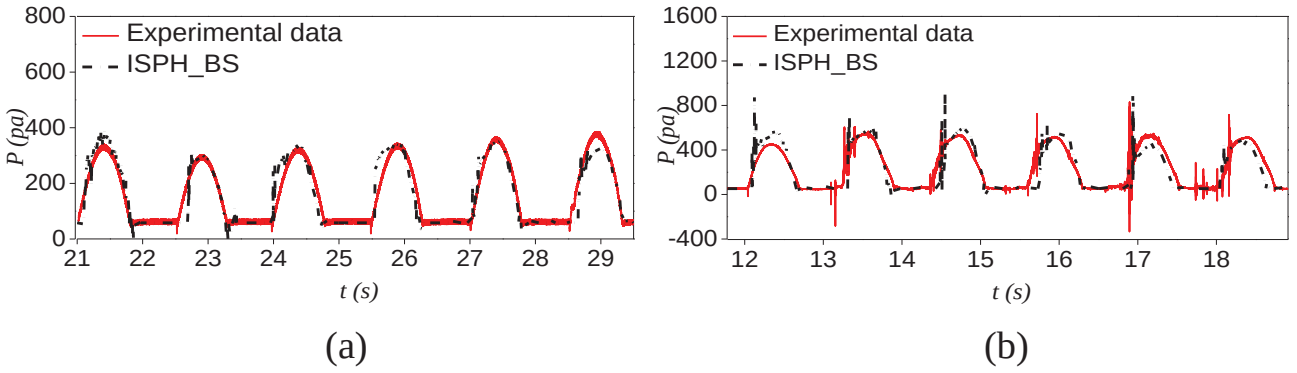

Fig. 27. Time history of impact pressure on waterline: (a) smaller amplitude wave; and (b) larger amplitude wave.

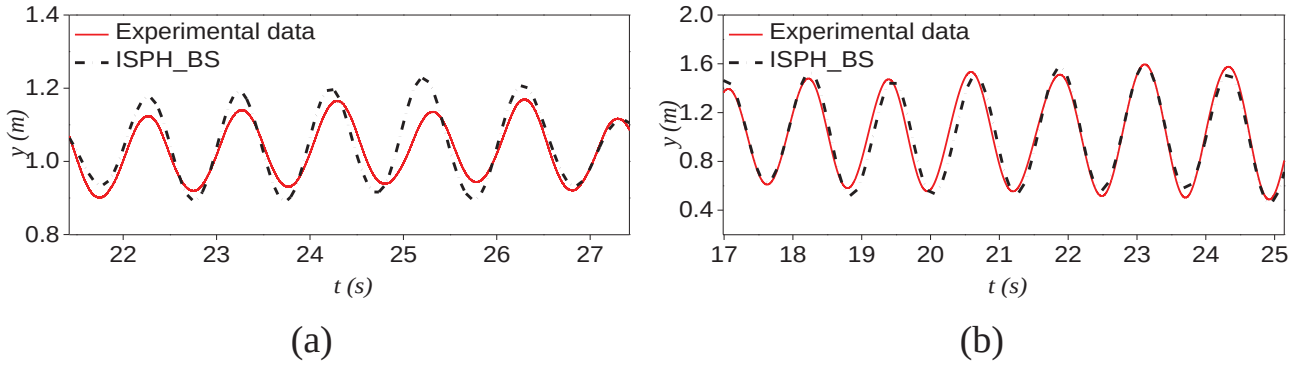

Fig. 28. Time history of heaving motion of the floating deck: (a) smaller amplitude wave; and (b) larger amplitude wave.

ISPH computations reproduced all of these satisfactorily. However, the heaving motion was overestimated for the smaller wave height, although the larger wave height case has been accurately predicted. As for the impact pressure, more serious experimental fluctuations are found inside the deck than the waterline region. This might be caused by the difficulty in the laboratory measurement due to the existence of air–water mixtures in this area. In comparison, the ISPH_BS computations achieved very stable pressure patterns in both situations, which could be attributed to the robustness of the pressure solution scheme using SFDI on the solid boundary. Compared with the smaller wave (H = 0.05 m), the larger wave (H = 0.1 m) doubled the wave impact pressures on inside the deck and the waterline. As a result, the heaving amplitude of the floating deck increases by 20%.

To further examine the influence of wave conditions on the impact pressure on the deck, Table 5 gives the maximum wave impact pressure on the inside of deck and the waterline for wave height H = 0.1 m and different wave periods T = 1.0, 1.2, 1.5 and 2.0 s. Both the experimental values and ISPH results are shown for a comparison. Similar studies were also carried out by assuming the deck structure being fixed and the corresponding results are shown in Table 6. By comparing Tables 5 and 6, we could see that the wave impact pressures generally decrease following an increase in the wave period, regardless of the deck being fixed or movable, or the location

Table 5
Experimental and ISPH impact pressures of the floating deck.

Test number	Wave period T (s)	Pressure of inside deck P (pa)		Pressure of waterline P (pa)	
		Experiment	ISPH	Experiment	ISPH
1	1.0	501.9	520.4	689.3	702.8
2	1.2	572.8	594.0	774.1	720.4
3	1.5	150.5	160.7	585.4	530.8
4	2.0	0.0	50.0	237.7	440.5

Table 6
Experimental and ISPH impact pressures of the fixed deck.

Test number	Wave period T (s)	Pressure of inside deck P (pa)		Pressure of waterline P (pa)	
		Experiment	ISPH	Experiment	ISPH
1	1.0	695.2	708.5	576.5	525.8
2	1.2	693.4	720.4	658.8	670.1
3	1.5	496.8	530.8	655.4	664.1
4	2.0	454.9	490.8	648.6	632.8

of pressure being taken inside the deck or on the waterline. Compared with the floating deck, the fixed deck greatly increases the impact pressure at the inside deck for all the wave conditions. However, on the waterline, the impact pressure of the fixed deck seems to be smaller than that of the floating one for the smaller wave period. Besides, the ISPH_BS computations are found to be very close to the experimental values for all the cases in Tables 5 and 6. This indicates the proposed model could provide a promising tool on the wave impact pressure predictions with engineering interest.

6. Conclusions

The paper proposed an accurate pressure solution method by applying the Simplified Finite Difference Interpolation scheme on the solid boundary to solve the PPE. By using a series of benchmark tests, it shows the improved numerical performance. Further application of the model to a self-designed laboratory experiment on the green water overtopping of a ship deck shows the ISPH_BS model can accurately reproduce the wave surface deformation, float motion as well as the wave impact pressure on different areas of the deck. The robustness of SFDI scheme coupled with the ISPH solver (ISPH_BS) lies in its high-order numerical nature and accurate treatment of the solid boundary, especially for the complex boundary without the need to use the mirror particles. This can effectively avoid the local mirroring inaccuracies when the solid boundary is in curved shape or the particle distributions are highly disordered. The proposed scheme can be easily extended to 3D and applicable to other projection-based particle methods such as the MPS.

However, we need to realise that the formulation adopted for the pressure gradient should be consistent both in the momentum balance and PPE for the comparison to be made on a fair basis. In the proposed ISPH_TS and ISPH_BS, the pressure gradients are computed by the SFDI in both cases, and also the inner fluid particles are involved in the PPE as well, but the difference lies in the treatment of solid boundary conditions during the solution of PPE. Specifically speaking, ISPH_TS uses the traditional ghost particles while ISPH_BS uses the high accuracy of SFDI near the solid boundary. Our major focus of this research is to explore the treatment of solid boundary in PPE to see how this influences the pressure prediction accuracy. Therefore, we did not fully address the inconsistency of pressure gradient used in the momentum balance and PPE, which should constitute a very promising future research direction.

Acknowledgement

This work is supported by the National Natural Science Foundation of China (Nos. 51739001, 51279041, 51379051, 51479087 and 51639004), Foundational Research Funds for the Central Universities (Nos. HEUCDZ1202, HEUCF 170104) and Defense Pre Research Funds Program (No. 9140A14020712CB01158), to which the authors are most grateful. Author S.D. Shao would like to acknowledge the National Key Basic Research Program of China (973 program, No. 2013CB036402). Author Q. Ma also thanks the Chang Jiang Visiting Chair Professorship Scheme of the Chinese Ministry of Education, hosted by HEU.

References

Adami, S., Hu, X.Y., Adams, N.A., 2012. A generalized wall boundary condition for smoothed particle hydrodynamics. J. Comput. Phys. 231 (21), 7057–7075.

Aly, A.M., Minh, T.N., Lee, S.W., 2015. Numerical analysis of liquid sloshing using the incompressible Smoothed Particle Hydrodynamics method. Adv. Mech. Eng. 7 (2), 765741.

Asai, M., Aly, A., Sonoda, Y., Sakai, Y., 2012. A stabilized incompressible SPH method by relaxing the density invariance condition. J. Appl. Math. 11, 2607–2645.

Bonet, J., Lok, T.S.L., 1999. Variational and momentum preservation aspects of smooth particle hydrodynamic formulations. Comput. Methods Appl. Mech. Eng. 180 (1–2), 97–115.

Bouscasse, B., Colagrossi, A., Marrone, S., Antuono, M., 2013. Nonlinear water wave interaction with floating bodies in SPH. J. Fluids Struct. 42, 112–129.

Canelas, R.B., Domínguez, J.M., Crespo, A.J.C., Gómez-Gesteira, M., Ferreira, R.M.L., 2015. A smooth particle hydrodynamics discretization for the modelling of free surface flows and rigid body dynamics. Int. J. Numer. Methods Fluids 78 (9), 581–593.

Dilts, G., 1999. Moving-least-squares-particle-hydrodynamics-I: consistency and stability. Int. J. Numer. Methods Eng. 44 (8), 1115–1155.

Faltinsen, O.M., 1977. Numerical solutions of transient nonlinear free-surface motion outside or inside moving bodies. In: Proceedings of the Second International Conference on Numerical Ship Hydrodynamics. University of California, Berkeley, pp. 347–357.

Gomez-Gesteira, M., Rogers, B.D., Crespo, A.J.C., Dalrymple, R.A., Narayanaswamy, M., Dominguez, J.M., 2012. SPHysics - development of a free-surface fluid solver - Part 1: theory and formulations. Comput. Geosci. 48, 289–299.

Gotoh, H., Khayyer, A., Ikari, H., Arikawa, T., Shimosako, K., 2014. On enhancement of Incompressible SPH method for simulation of violent sloshing flows. Appl. Ocean Res. 46, 104–115.

Gotoh, H., Khayyer, A., 2016. Current achievements and future perspectives for projection-based particle methods with applications in ocean engineering. J. Ocean Eng. Mar. Energy 2 (3), 251–278.

Gui, Q., Dong, P., Shao, S., 2015. Numerical study of PPE source term errors in the incompressible SPH models. Int. J. Numer. Methods Fluids 77 (6), 358−379.

Ikari, H., Gotoh, H., Khayyer, A., 2011. Numerical simulation on moored floating body in wave by improved MPS method. In: Coastal Structures 2011, vols. 1 & 2, pp. 308−317.

Jun, C.W., Sohn, J.H., Lee, K.C., 2015. Dynamic analysis of a floating body in the fluid by using the smoothed particle hydrodynamics. J. Mech. Sci. Technol. 29 (7), 2607−2613.

Koshizuka, S., Nobe, A., Oka, Y., 1998. Numerical analysis of breaking waves using the moving particle semi-implicit method. Int. J. Numer. Meth. Fluids 26, 751−769.

Lee, B.H., Jeong, S.M., Hwang, S.C., Park, J.C., Kim, M.H., 2013. A particle simulation of 2-D vessel motions interacting with liquid-sloshing cargo. CMES Comput. Model. Eng. Sci. 91 (1), 43−63.

Leroy, A., Violeau, D., Ferrand, M., Kassiotis, C., 2014. Unified semi-analytical wall boundary conditions applied to 2-D incompressible SPH. J. Comput. Phys. 261, 106−129.

Lin, P.Z., Liu, P.L.F., 1998. A numerical study of breaking waves in the surf zone. J. Fluid Mech. 359, 239−264.

Liu, M.B., Liu, G.R., 2006. Restoring particle consistency in smoothed particle hydrodynamics. Appl. Numer. Math. 56, 19−36.

Liu, W.K., Jun, S., Zhang, Y.F., 1995. Reproducing kernel particle methods. Int. J. Numer. Methods Fluids 20, 1081−1106.

Liu, X., Lin, P.Z., Shao, S.D., 2014. An ISPH simulation of coupled structure interaction with free surface flows. J. Fluids Struct. 48, 46−61.

Ma, Q.W., 2008. A new meshless interpolation scheme for MLPG_R method. CMES-Comput. Model. Eng. Sci. 23 (2), 75−89.

Macia, F., Antuono, M., Gonzlez, L.M., Colagrossi, A., 2011. Theoretical analysis of the no-slip boundary condition enforcement in SPH methods. Prog. Theor. Phys. 125, 1091−1121.

Marrone, S., Antuono, M., Colagrossi, A., Colicchio, G., Le Touze, D., Graziani, G., 2011. delta-SPH model for simulating violent impact flows. Comput. Methods Appl. Mech. Eng. 200 (13−16), 1526−1542.

Marrone, S., Colagrossi, A., Antuono, M., Colicchio, G., Graziani, G., 2013. An accurate SPH modeling of viscous flows around bodies at low and moderate Reynolds numbers. J. Comput. Phys. 245, 456−475.

Mei, C.C., Black, J.L., 1969. Scattering of surface waves by rectangular obstacles in waters of finite depth. J. Fluid Mech. 38, 499−511.

Monaghan, J.J., Kos, A., Issa, N., 2003. Fluid motion generated by impact. J. Water Port Coast Ocean Eng. 129, 250−259.

Najafi-Jilani, A., Rezaie-Mazyak, A., 2011. Numerical investigation of floating breakwater movement using SPH method. Int. J. Nav. Archit. Ocean Eng. 3 (2), 122−125.

Oger, G., Doring, M., Alessandrini, B., Ferrant, P., 2007. An improved SPH method: towards higher order convergence. J. Comput. Phys. 225 (2), 1472−1492.

Quinlan, N.J., Basa, M., Lastiwka, M., 2006. Truncation error in mesh-free particle methods. Int. J. Numer. Meth. Eng. 66, 2064−2085.

Ren, B., He, M., Dong, P., Wen, H.J., 2015. Nonlinear simulations of wave-induced motions of a freely floating body using WCSPH method. Appl. Ocean Res. 50, 1−12.

Rudman, M., Cleary, P.W., 2016. The influence of mooring system in rogue wave impact on an offshore platform. Ocean Eng. 115, 168−181.

Shadloo, M.S., Zainali, A., Sadek, S.H., Yildiz, M., 2011. Improved Incompressible Smoothed Particle Hydrodynamics method for simulating flow around bluff bodies. Comput. Methods Appl. Mech. Eng. 200 (9−12), 1008−1020.

Shao, S.D., Lo, E.Y.M., 2003. Incompressible SPH method for simulating Newtonian and non-Newtonian flows with a free surface. Adv. Water Resour. 26 (7), 787−800.

Sriram, V., Ma, Q.W., 2012. Improved MLPG_R method for simulating 2D interaction between violent waves and elastic structures. J. Comput. Phys. 231 (22), 7650−7670.

Takeda, H., Miyama, S.M., Sekiya, M., 1994. Numerical-simulation of viscous-flow by smoothed particle hydrodynamics. Prog. Theor. Phys. 92 (5), 939−960.

Yildiz, M., Rook, R.A., Suleman, A., 2009. SPH with the multiple boundary tangent method. Int. J. Numer. Methods Eng. 77 (10), 1416−1438.

Zhang, S., Morita, K., Fukuda, K., Shirakawa, N., 2006. An improved MPS method for numerical simulations of convective heat transfer problems. Int. J. Numer. Methods Fluids 51 (1), 31−47.

Zheng, X., Ma, Q.W., Duan, W.Y., 2014. Incompressible SPH method based on Rankine source solution for violent water wave simulation. J. Comput. Phys. 276, 291−314.

Zheng, X., Shao, S.D., Khayyer, A., Duan, W.Y., Ma, Q.W., Liao, K.P., 2017. Corrected first-order derivative ISPH in water wave simulations. Coast. Eng. J. 59 (1), 1750010.